INTERNATIONAL JOURNAL FOR NUMERICAL METHODS IN FLUIDS
Int. J. Numer. Meth. Fluids 2007; **55**:387–406
Published online 20 March 2007 in Wiley InterScience (www.interscience.wiley.com). DOI: 10.1002/fld.1472

The (9,5) HOC formulation for the transient Navier–Stokes equations in primitive variable

Jiten C. Kalita[1,*,†,§] and Shuvam Sen[2,‡,¶]

[1]*Department of Mathematics, Indian Institute of Technology, Guwahati 781039, India*
[2]*Department of Mathematical Sciences, Tezpur University, Tezpur 784028, India*

SUMMARY

We recently proposed an improved (9,5) higher order compact (HOC) scheme for the unsteady two-dimensional (2-D) convection–diffusion equations. Because of using only five points at the current time level in the discretization procedure, the scheme was seen to be computationally more efficient than its predecessors. It was also seen to capture very accurately the solution of the unsteady 2-D Navier–Stokes (N–S) equations for incompressible viscous flows in the stream function–vorticity ($\psi - \omega$) formulation.

In this paper, we extend the scope of the scheme for solving the unsteady incompressible N–S equations based on primitive variable formulation on a collocated grid. The parabolic momentum equations are solved for the velocity field by a time-marching strategy and the pressure is obtained by discretizing the elliptic pressure Poisson equation by the steady-state form of the (9,5) scheme with the Neumann boundary conditions. In particular, for pressure, we adopt a strategy on the collocated grid in conjunction with ideas borrowed from the staggered grid approach in finite volume. We first apply this extension to a problem having analytical solution and then to the famous lid-driven square cavity problem. We also apply our formulation to the backward-facing step problem to see how the method performs for external flow problems. The results are presented and are compared with established numerical results. This new approach is seen to produce excellent comparison in all the cases. Copyright © 2007 John Wiley & Sons, Ltd.

Received 4 October 2006; Revised 31 January 2007; Accepted 1 February 2007

KEY WORDS: 2-D; unsteady; convection–diffusion; HOC; N–S equations; accuracy

*Correspondence to: Jiten C. Kalita, Department of Mathematics, IIT, Guwahati 781039, India.
†E-mail: jiten@iitg.ernet.in
‡E-mail: shuvam@tezu.ernet.in
§Assistant Professor.
¶Lecturer.

1. INTRODUCTION

The transient two-dimensional (2-D) incompressible Navier–Stokes (N–S) equations in the traditional primitive variable (velocity–pressure) formulation is

$$\frac{\partial u}{\partial x}+\frac{\partial v}{\partial y}=0 \tag{1}$$

$$\frac{\partial u}{\partial t}+u\frac{\partial u}{\partial x}+v\frac{\partial u}{\partial y}-\frac{1}{Re}\nabla^2 u=-\frac{\partial p}{\partial x} \tag{2}$$

$$\frac{\partial v}{\partial t}+u\frac{\partial v}{\partial x}+v\frac{\partial v}{\partial y}-\frac{1}{Re}\nabla^2 v=-\frac{\partial p}{\partial y} \tag{3}$$

where u, v are velocities along x-, y-directions respectively, p is the pressure, t is the time and Re is the Reynolds number given by $Re=Lu_0/v$, where L is some characteristic length, u_0 some characteristic velocity and v is the kinematic viscosity. Though this formulation accurately represents the fluid flow phenomenon, its direct solution traditionally has been difficult to obtain due to the pressure term in Equations (2) and (3). Partly in order to avoid handling the pressure variable, an alternative formulation using stream function and vorticity has been used for several decades. The alternative formulation introduces the stream function ψ and vorticity ω and is written as

$$\psi_{xx}+\psi_{yy}=-\omega(x, y) \tag{4}$$

$$\omega_t+(u\omega_x+v\omega_y)=\frac{1}{Re}(\omega_{xx}+\omega_{yy}) \tag{5}$$

The velocity components are defined as

$$u(x, y)=\psi_y, \quad v(x, y)=-\psi_x \tag{6}$$

The last several decades have seen several attempts on developing finite-difference schemes for the transient N–S equations, both in the primitive variable as well as in ψ–ω formulations. Amongst them higher order compact (HOC) finite-difference schemes have become quite popular as against the other lower order accurate schemes which require high mesh refinements and hence are computationally inefficient. On the other hand, the higher order accuracy of the HOC methods combined with the compactness of the difference stencil yields highly accurate numerical solutions on relatively coarser grids with greater computational efficiency. Most of these HOC schemes were developed for the 2-D convection–diffusion equations in steady state which were extended later on to solve the steady-state N–S equations. Very few of them [1] were in the primitive variable formulations. Recently, Kalita *et al.* developed a few classes of HOC [2, 3] schemes for the 2-D convection–diffusion equations which were seen to capture very accurately and efficiently transient flows governed by the incompressible N–S equations. However like most of the other HOC schemes, they utilized the ψ–ω formulation only.

The present work is an attempt to solve the transient N–S equations in the primitive variable formulations using the recently developed (9,5) scheme [3] on collocated grids. In the process we also rope in a finite volume staggered grid approach on the collocated grid for the treatment of the pressure variable. To the best of our knowledge, this is perhaps the only attempt to solve the

DOI: 10.1002/fld

N–S equations in the primitive variable form by a transient HOC scheme on a collocated grid. We firstly apply the proposed procedure on a problem having analytical solution for which we also carry out error analysis. Then we apply it to the famous lid-driven square cavity problem, both the unsteady and time-marching steady-state case. Finally to test how the present method performs for an external flow situation we apply it to the backward-facing step problem. Results are compared with those obtained with other established schemes for both primitive variable and ψ–ω formulations. For the first problem, our numerical results are extremely close to the analytical ones, whereas for the cavity and step problems, our solutions agree very well, both qualitatively and quantitatively with already published results.

The paper has been arranged in four sections. Section 2 deals with discretization and issues related to it, particularly the treatment of the pressure equation at the interior and at the boundary, Section 3 with the numerical test cases and finally, Section 4 summarizes the whole work.

2. DISCRETIZATION AND NUMERICAL PROCEDURE

The transient 2-D convection–diffusion equation in the variable ϕ in some convex domain Ω (assumed rectangular here) with boundary $\partial\Omega$ may be written as

$$a\frac{\partial\phi}{\partial t} - \nabla^2\phi + c(x, y, t)\frac{\partial\phi}{\partial x} + d(x, y, t)\frac{\partial\phi}{\partial y} = g(x, y, t) \tag{7}$$

where a is a constant, c and d are the convection coefficients and g is a forcing function. In Reference [3], Kalita and Chhabra proposed an HOC scheme for Equation (7) at the (i, j)th point (x_i, y_j) which is given by

$$\begin{aligned} &a\left[1 + \left(\frac{\Delta x^2}{12} - \frac{\Delta t}{2a}\right)(\delta_x^2 - c_{i,j}\delta_x) + \left(\frac{\Delta y^2}{12} - \frac{\Delta t}{2a}\right)(\delta_y^2 - d_{i,j}\delta_y)\right]\delta_t^+\phi_{i,j} \\ &+ (-\alpha_{i,j}\delta_x^2 - \beta_{i,j}\delta_y^2 + C_{i,j}\delta_x + D_{i,j}\delta_y)\phi_{i,j} \\ &-\frac{\Delta x^2 + \Delta y^2}{12}(\delta_x^2\delta_y^2 - c_{i,j}\delta_x\delta_y^2 - d_{i,j}\delta_x^2\delta_y - \gamma_{i,j}\delta_x\delta_y)\phi_{i,j} = G_{i,j} \end{aligned} \tag{8}$$

where Δx, Δy are the uniform step lengths in the x- and y-directions, respectively, and Δt is the uniform time step. The details of the coefficients and finite difference operators appearing in (8) can be found in [3]. The order of accuracy of this unconditionally stable implicit scheme is $O(\Delta t^2, \Delta x^4, \Delta y^4)$. As it utilizes nine points at the previous and five points at the current time level, it was termed a (9, 5) scheme.

To solve the N–S equations, firstly we discretize the momentum equations (2) and (3) using (8) with $a = Re$, $c = Re\,u$, $d = Re\,v$ and $g = Re\,\partial p/\partial x$ or $Re\,\partial p/\partial y$; for both the equations, we use the Dirichlet conditions for u and v at the boundaries. It is to be noted that since analytical expressions are not known for p, we must approximate the pressure gradients numerically. For this, we may use central difference approximations at the interior and standard one sided first order approximations at the boundaries. One can also use the strategy applied in Reference [4] for the gradient source term in order to obtain a fourth order compact approximation. Once the momentum equations (2)–(3) are solved, we proceed to find pressure p as follows:

DOI: 10.1002/fld

By differentiating Equation (2) with respect to x and (3) with respect to y, and adding, we get the familiar pressure Poisson equation (PPE)

$$\nabla^2 p = w \tag{9}$$

where $w = -(uu_x + vu_y)_x - (uv_x + vv_y)_y - D_t + (D_{xx} + D_{yy})/Re$ with $D = u_x + v_y$.

Although a staggered grid approach [5–7] is quite effective in handling the PPE, but it has an inherent complexity related to book-keeping. On the other hand, collocated grid is much simpler to use even when dealing with complex solution domains. Reasonably accurate solutions are obtained from the PPE with the Neumann boundary conditions, but only when some compatibility condition is satisfied. To discretize (9), we use the steady-state form of (7) in conjunction with the approaches suggested in [8, 9] for the treatment of the source term w in (9) and the Neumann boundary conditions. At the interior, the steady-state form of (8) yields

$$\left[\delta_x^2 + \delta_y^2 + \frac{\Delta x^2 + \Delta y^2}{12}\delta_x^2\delta_y^2\right] p_{i,j} = \left[1 + \frac{\Delta x^2}{12}\delta_x^2 + \frac{\Delta y^2}{12}\delta_y^2\right] w_{i,j} \tag{10}$$

where $w_{i,j}$ is obtained by following the approach shown in [8] and is expressed as

$$\begin{aligned} w_{i,j} = &-(u_{i+1,j}+u_{i,j})(u_{i+1,j}-u_{i,j})/2 - (v_{i+1,j}+v_{i,j})(u_{i+1,j+1}+u_{i,j+1} - u_{i+1,j-1} - u_{i,j-1})/8 \\ &+ (u_{i,j}+u_{i-1,j})(u_{i,j} - u_{i-1,j})/2+(v_{i,j}+v_{i-1,j})(u_{i,j+1}+u_{i-1,j+1} - u_{i,j-1} - u_{i-1,j-1})/8 \\ &- (u_{i,j+1}+u_{i,j})(v_{i+1,j+1}+v_{i+1,j} - v_{i-1,j+1} - v_{i-1,j})/8 - (v_{i,j+1}+v_{i,j})(v_{i,j+1} - v_{i,j})/2 \\ &+ (u_{i,j}+u_{i,j-1})(v_{i+1,j}+v_{i+1,j-1} - v_{i-1,j} - v_{i-1,j-1})/8+(v_{i,j} + v_{i,j-1})(v_{i,j} - v_{i,j-1})/2 \\ &+ \frac{1}{Re}(D_{i+1,j} + D_{i-1,j} + D_{i,j+1} + D_{i,j-1} - 4D_{i,j}) + \Delta x\Delta y\frac{D_{i,j}}{\Delta t} \end{aligned} \tag{11}$$

Assuming constant velocities along the boundaries, Equations (2)–(3) reduce to

$$\frac{\partial p}{\partial x} = -u\frac{\partial u}{\partial x} - v\frac{\partial u}{\partial y} + \frac{1}{Re}\nabla^2 u \tag{12}$$

$$\frac{\partial p}{\partial y} = -u\frac{\partial v}{\partial x} - v\frac{\partial v}{\partial y} + \frac{1}{Re}\nabla^2 v \tag{13}$$

The finite-difference approximations for the pressure Neumann boundary conditions (12)–(13) on a grid of size $m \times n$ are as follows:

On the left boundary, $\forall\, 1 \leqslant j \leqslant n$:

$$\begin{aligned} p_{2,j} - p_{1,j} = &-(u_{2,j} + u_{1,j})(u_{2,j} - u_{1,j})/2 - (v_{2,j}+v_{1,j})(u_{2,j+1}+u_{1,j+1} - u_{2,j-1} - u_{1,j-1})/8 \\ &+ \frac{1}{Re}\left[-\frac{(v_{2,j+1} - v_{2,j-1}) - (v_{1,j+1} - v_{1,j-1})}{2\Delta y}\right] \\ &+ \frac{1}{Re}\left[\frac{(u_{2,j+1} - 2u_{2,j} + u_{2,j-1}) + (u_{1,j+1} - 2u_{1,j} + u_{1,j-1})}{2\Delta y}\right] \\ &+ \frac{1}{Re}\left(D_{2,j} - D_{1,j}\right) \end{aligned} \tag{14}$$

DOI: 10.1002/fld

On the right boundary, $\forall\, 1 \leqslant j \leqslant n$:

$$\begin{aligned} p_{m-1,j} - p_{m,j} &= (u_{m-1,j} + u_{m,j})(u_{m,j} - u_{m-1,j})/2 \\ &\quad + (v_{m,j} + v_{m-1,j})(u_{m-1,j+1} + u_{m,j+1} - u_{m-1,j-1} - u_{m,j-1})/8 \\ &\quad + \frac{1}{Re}\left[-\frac{(v_{m-1,j+1} - v_{m-1,j-1}) - (v_{m,j+1} - v_{m,j-1})}{2\Delta y}\right] \\ &\quad + \frac{1}{Re}\left[-\frac{(u_{m-1,j+1} - 2u_{m-1,j} + u_{m-1,j-1}) + (u_{m,j+1} - 2u_{m,j} + u_{m,j-1})}{2\Delta y}\right] \\ &\quad + \frac{1}{Re}\left(D_{m-1,j} - D_{m,j}\right) \end{aligned} \tag{15}$$

On the bottom, $\forall\, 1 \leqslant i \leqslant m$:

$$\begin{aligned} p_{i,2} - p_{i,1} &= -(u_{i,2} + u_{i,1})(v_{i+1,2} + v_{i+1,1} - v_{i-1,2} - v_{i-1,1})/8 - (v_{i,2} + v_{i,1})(v_{i,2} - v_{i,1})/2 \\ &\quad + \frac{1}{Re}\left[-\frac{(v_{i+1,2} - 2v_{i,2} + v_{i-1,2}) + (v_{i+1,1} - 2v_{i,1} + v_{i-1,1})}{2\Delta x}\right] \\ &\quad + \frac{1}{Re}\left[-\frac{(u_{i+1,2} - u_{i-1,2}) - (u_{i+1,1} - u_{i-1,1})}{2\Delta x}\right] + \frac{1}{Re}(D_{i,2} - D_{i,1}) \end{aligned} \tag{16}$$

Finally at the top boundary, $\forall\, 1 \leqslant i \leqslant m$:

$$\begin{aligned} p_{i,n-1} - p_{i,n} &= (u_{i,n-1} + u_{i,n})(v_{i+1,n-1} - v_{i+1,n} - v_{i-1,n-1} - v_{i-1,n-1})/8 \\ &\quad + (v_{i,n} + v_{i,n-1})(v_{i,n-1} - v_{i,n-1})/2 \\ &\quad + \frac{1}{Re}\left[-\frac{(v_{i+1,n-1} - 2v_{i,n-1} + v_{i-1,n-1}) + (v_{i+1,n} - 2v_{i,n} + v_{i-1,n})}{2\Delta x}\right] \\ &\quad + \frac{1}{Re}\left[-\frac{(u_{i+1,n-1} - u_{i-1,n-1}) - (u_{i+1,n} - u_{i-1,n})}{2\Delta x}\right] \\ &\quad + \frac{1}{Re}\left(D_{i,n-1} - D_{i,n}\right) \end{aligned} \tag{17}$$

Note that, for the continuity equation (1) to be satisfied at the next time step, $D_{i,j}^{(n+1)}$ is set equal to zero as in [8], but $D_{i,j}(\equiv D_{i,j}^{(n)})$ is retained at each time step to overcome non-linear instabilities. But unlike [8, 9], we have retained the term $(D_{xx} + D_{yy})/Re$ on the RHS of (9) which along with (12)–(13) yields the correct pressure field.

DOI: 10.1002/fld

After discretization, the momentum equations and the PPE finally reduce to the single matrix forms

$$A_1\mathbf{u}^{(n+1)} = \mathbf{f}_1(\mathbf{u}^{(n)}, \mathbf{v}^{(n)}, \mathbf{p}^{(n)}) \tag{18}$$

$$A_2\mathbf{v}^{(n+1)} = \mathbf{f}_2(\mathbf{u}^{(n)}, \mathbf{v}^{(n)}, \mathbf{p}^{(n)}) \tag{19}$$

$$A_3\mathbf{p}^{(n+1)} = \mathbf{f}_3(\mathbf{u}^{(n+1)}, \mathbf{v}^{(n+1)}, \mathbf{u}^{(n)}, \mathbf{v}^{(n)}) \tag{20}$$

where the coefficient matrices A_i $(1 \leqslant i \leqslant 3)$ are asymmetric sparse matrices. For a grid of size $m \times n$, A_i has a dimension mn, and $\mathbf{u}^{(n)}$, $\mathbf{u}^{(n+1)}$, $\mathbf{v}^{(n)}$, $\mathbf{v}^{(n+1)}$, $\mathbf{p}^{(n)}$, $\mathbf{p}^{(n+1)}$, $\mathbf{f}_i$ $(1 \leqslant i \leqslant 3)$ are mn-component vectors.

The next step now is to solve Equations (18)–(20) with iterative methods. As the coefficient matrix A is not generally diagonally dominant, conventional iterative methods such as Gauss–Seidel cannot be used. In order to solve these systems the biconjugate gradient stabilized method (BiCGStab) [10–13] is used here without preconditioning.

To compute the time accurate or time-marching steady-state solutions of the N–S equations, we employ an outer-inner iteration procedure. After some suitable initialization strategy, in a typical outer temporal cycle, (18)–(20) are solved using BiCGStab. Once all the values of u, v and p are computed at a particular time step, the temporal outer iteration is complete. The stopping criteria for the inner iterations are different for different problems (see Sections 3.1, 3.2 and 3.3). All of our computations were carried out on a Pentium 4-based PC with 512 MB RAM using double precision floating point arithmetic.

3. NUMERICAL EXAMPLES

In order to validate the proposed scheme and test its robustness, we apply it to three unsteady 2-D problems. These are: (i) the flow decayed by viscosity; (ii) the flow in the lid-driven square cavity; and (iii) the backward-facing step problem. As the first problem has analytical solutions, we use exact initial data whereas for the other two problems, zero initial data were used in all the computations, unless otherwise specified.

3.1. Problem 1: flow decayed by viscosity

We consider the flow decayed by viscosity problem [2, 14–17] governed by the 2-D N–S equations (1)–(3) in the square $0 \leqslant x, y \leqslant \pi$, which has analytical solutions given by

$$u(x, y, t) = -\cos x \sin y \, \mathrm{e}^{-2t/Re}, \quad v(x, y, t) = \sin x \cos y \, \mathrm{e}^{-2t/Re} \tag{21}$$

and

$$p(x, y, t) = -\tfrac{1}{4}(\cos 2x + \cos 2y)\mathrm{e}^{-4t/Re} \tag{22}$$

The initial and boundary conditions for u, v and p can be found from (21) and (22).

We present our results computed on grid sizes ranging from 21×21 to 101×101 for different Reynolds numbers in Table I and Figures 1–3. That the flow decays with viscosity is obvious from Figure 1 where the exact and numerical surface and contour plots of the horizontal velocity u are shown for $Re = 100$ at two different times $t = 2.0$ and 20.0. Figure 2 displays similar contour plots for vertical velocity v. One can hardly distinguish the numerical solutions from the analytical

DOI: 10.1002/fld

Table I. Convergence rate of the (9,5) HOC scheme.

Grid	Maximum|error| (at $t=2.0$)	Rate	Maximum|error| (at $t=4.0$)	Rate	Maximum|error| (at $t=20.0$)	Rate
			$Re=50$			
			For u			
21×21	0.00273188		0.00231621		0.00062696	
		3.280		3.216		2.868
41×41	0.00028127		0.00024928		0.00008586	
		2.591		2.634		2.869
81×81	0.00004669		0.00004016		0.00001175	
			For v			
21×21	0.00430123		0.00376310		0.00124538	
		2.975		3.011		3.326
41×41	0.00054709		0.00046684		0.00012422	
		3.316		3.341		3.344
81×81	0.00005495		0.00004606		0.00001223	
			For p			
21×21	0.01344523		0.01112516		0.00253587	
		2.226		2.164		1.742
41×41	0.00287319		0.00248328		0.00075799	
		1.670		1.681		1.767
81×81	0.00090305		0.00077430		0.00022264	
			$Re=100$			
			For u			
61×61	0.00016589		0.00015502		0.00008922	
		2.601		2.479		2.584
81×81	0.00007849		0.00007598		0.00004242	
		2.359		2.539		2.592
101×101	0.00004636		0.00004312		0.00002390	
			For v			
61×61	0.00026516		0.00024557		0.00013109	
		3.192		2.978		3.112
81×81	0.00010584		0.00010424		0.00005356	
		2.535		2.845		2.952
101×101	0.00006011		0.00005525		0.00002772	
			For p			
61×61	0.00163631		0.00151879		0.00082403	
		1.712		1.817		1.815
81×81	0.00099980		0.00090062		0.00048890	
		2.086		1.952		1.953
101×101	0.00062765		0.00058260		0.00031618	

DOI: 10.1002/fld

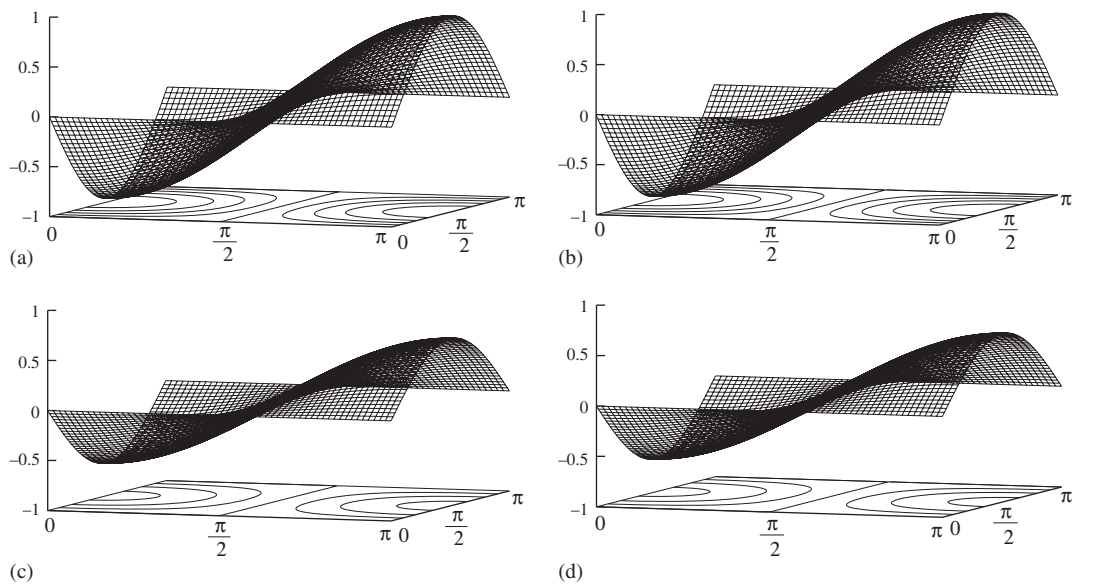

Figure 1. Surface and contour plots horizontal velocity for problem 1 ($Re = 100,\ 61 \times 61$ grid): (a) numerical at $t = 2.0$; (b) exact at $t = 2.0$; (c) numerical at $t = 20.0$; and (d) exact at $t = 20.0$.

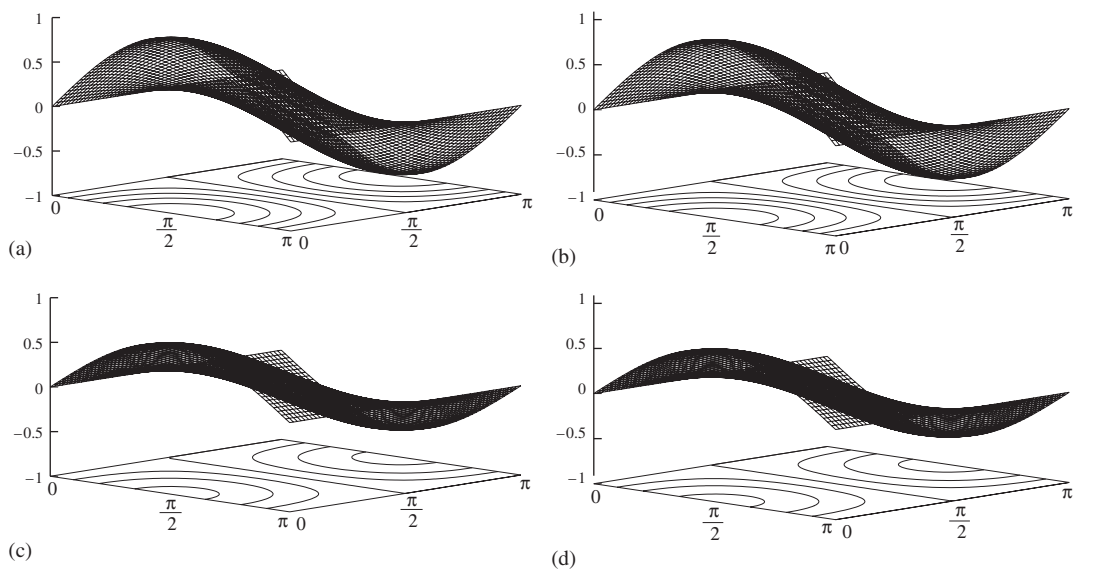

Figure 2. Surface and contour plots vertical velocity for problem 1 ($Re = 100,\ 61 \times 61$ grid): (a) numerical at $t = 2.0$; (b) exact at $t = 2.0$; (c) numerical at $t = 20.0$; and (d) exact at $t = 20.0$.

DOI: 10.1002/fld

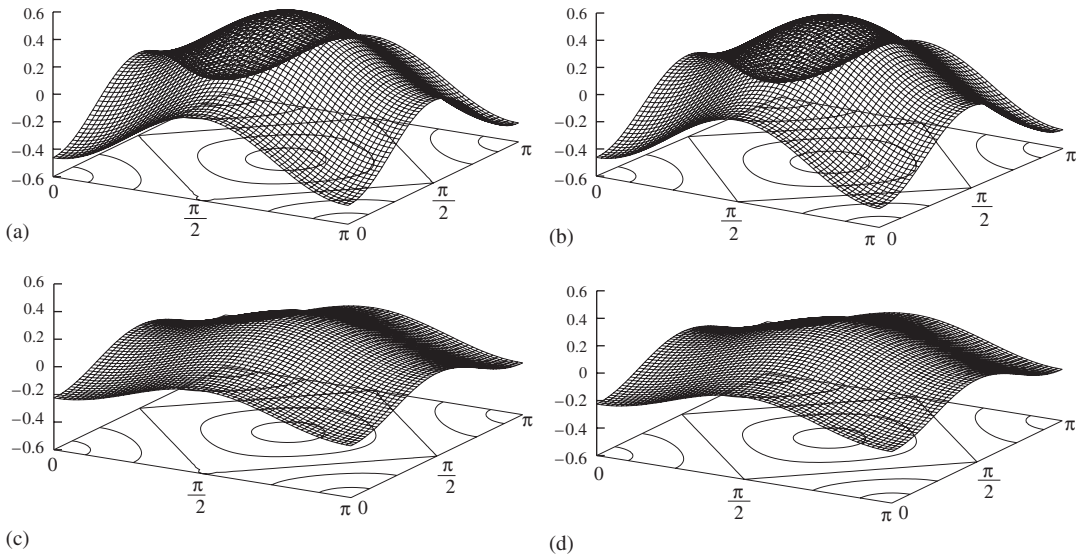

Figure 3. Surface and contour plots pressure for problem 1 ($Re = 100$, 61×61 grid): (a) numerical at $t = 2.0$; (b) exact at $t = 2.0$; (c) numerical at $t = 20.0$; and (d) exact at $t = 20.0$.

ones. This is also obvious from Figure 3 where the numerical and exact contour plots for p, at times $t = 2.0$ and 20.0 for $Re = 100$, obtained with a time step $\Delta t = 0.00025$ and space lengths $\Delta x = \Delta y = \pi/60$ are almost identical. Table I summarizes the maximum absolute errors for the velocities and the pressure on three grid sizes. Although the rate is on the expected line for the velocities, a lower rate of convergence can be seen for p. The lower convergence rate for p may be attributed to the fact that we are approximating pressure gradients by a second order central difference scheme at the interior points. In all the computations, the stopping criterion for the BiCGStab inner iterations was set at 0.5×10^{-6}.

3.2. Test problem 2: the lid-driven square cavity problem

Next we consider the 2-D lid-driven square cavity problem. This problem, over the years, has become the most frequently used benchmark problem for the assessment of numerical methods [2, 4, 17–20], particularly the steady-state solution of the incompressible fluid flows governed by the N–S equations (1)–(3). This problem is of great scientific interest because it displays almost all fluid mechanical phenomena for incompressible viscous flows in the simplest of geometric settings. The cavity is defined as the square $0 \leqslant x, y \leqslant 1$. The fluid motion is generated by the sliding motion of the top wall of the cavity ($y = 1$) in its own plane from left to right. Boundary conditions on the top wall are given as $u = 1$, $v = 0$. On all other walls of the cavity the velocities are zero ($u = v = 0$). The moving wall generates vorticity which diffuses inside the cavity and this diffusion is the driving mechanism of the flow. At high Re, several secondary and tertiary vortices begin to appear, whose characteristics depend on Re.

We obtain the steady-state solutions using a time-marching strategy. The steady state is assumed to reach when the maximum ϕ-error (ϕ being either u or v) between two successive outer temporal

DOI: 10.1002/fld

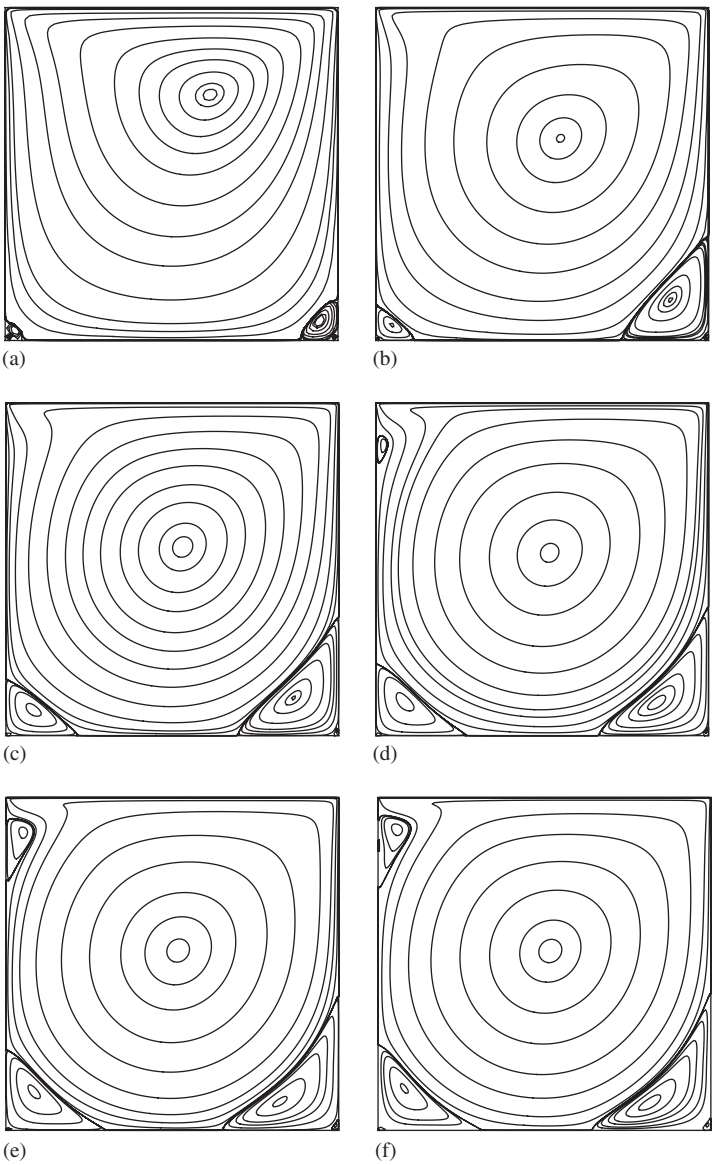

Figure 4. The steady-state streamlines for the lid-driven cavity flow for: (a) $Re = 100$; (b) $Re = 400$; (c) $Re = 1000$; (d) $Re = 2000$; (e) $Re = 3200$; and (f) $Re = 4000$.

iteration steps is smaller than 1.0×10^{-7}; the same tolerance limit was set for the inner BiCGStab iterations as well. Once the steady state is reached stream function values are post-processed using (4) with discretization similar to (10).

In Figure 4, we present the well-known stream function contours for $100 \leqslant Re \leqslant 4000$. All these graphs exhibit the typical separations and secondary vortices at the bottom corners of the cavity as

DOI: 10.1002/fld

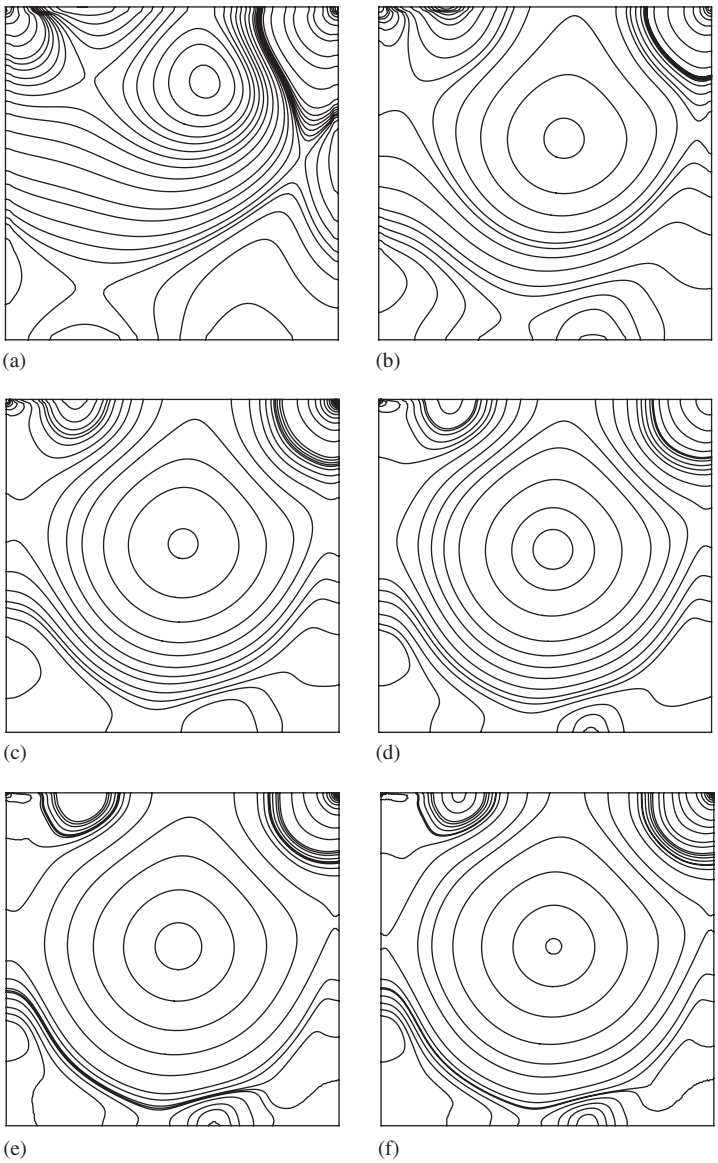

Figure 5. The steady-state pressure contours for the lid-driven cavity flow for: (a) $Re = 100$; (b) $Re = 400$; (c) $Re = 1000$; (d) $Re = 2000$; (e) $Re = 3200$; and (f) $Re = 4000$.

well as at the top left (which is visible here for $Re = 2000$ onwards). We can also see evolution of tertiary vortices for Reynolds number as low as $Re = 100$ which concurs with the comments made in Reference [21]. These stream function profiles match with the benchmark results of Ghia *et al.* [18] and other established results [19, 20, 22, 23] thereby confirming that our formulation yields quantitatively accurate solutions.

DOI: 10.1002/fld

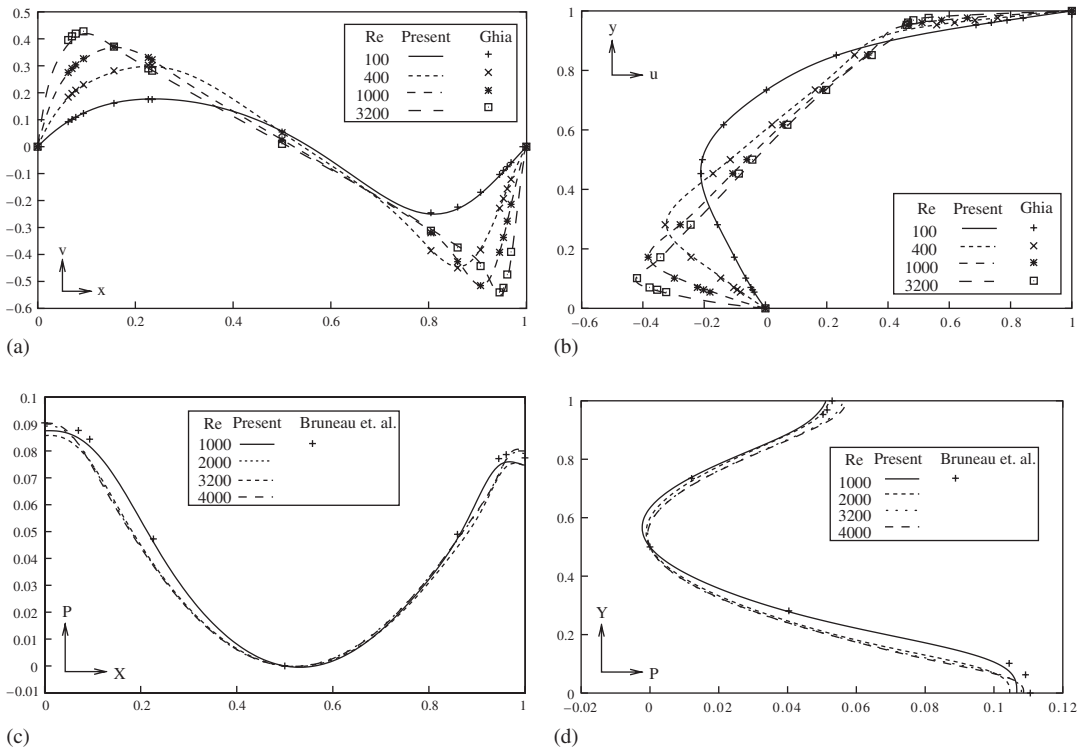

Figure 6. Comparisons of steady state for the lid-driven square cavity flow: (a) vertical velocity along the horizontal centreline; (b) horizontal velocity along the vertical centreline; (c) pressure along the horizontal centreline; and (d) pressure along the vertical centreline.

Figure 5 exhibits pressure contours for $100 \leqslant Re \leqslant 4000$. The contours when compared with established results [8, 20, 23] give excellent comparison. Figures 6(a) and (b) exhibit comparisons of the vertical velocities on the horizontal centreline and the horizontal velocities on the vertical centreline of the square cavity for $100 \leqslant Re \leqslant 3200$ with those of Ghia *et al.* [18]. In each case, our velocity profiles match very well with [18]. Figures 6(c) and (d) exhibit pressure on the horizontal centreline and the vertical centreline, respectively, of the square cavity. For $Re = 1000$ we compare our results with those obtained by Bruneau and Saad [20] on a 1024×1024 grid. Again we obtain a pretty consistent comparison. In Figure 7, we show the surface plot of the divergence of velocity for $Re = 1000$. As can be seen from the plot the divergence vanishes everywhere except at the top two corners of the cavity which is due to the discontinuities of the horizontal velocities at those points.

In Table II, we provide quantitative data comparison of our solutions. Here we present our fine grid steady-state data for the primary, secondary and tertiary vortex centres and compare them with the well established work of Ghia *et al.* [18]. Our results again prove to be an excellent match. In Table III, global quantities such as the total kinetic energy E and the enstrophy Z are being provided. Also as an addition, we provide the drag coefficient C_d on the top. These quantities are

DOI: 10.1002/fld

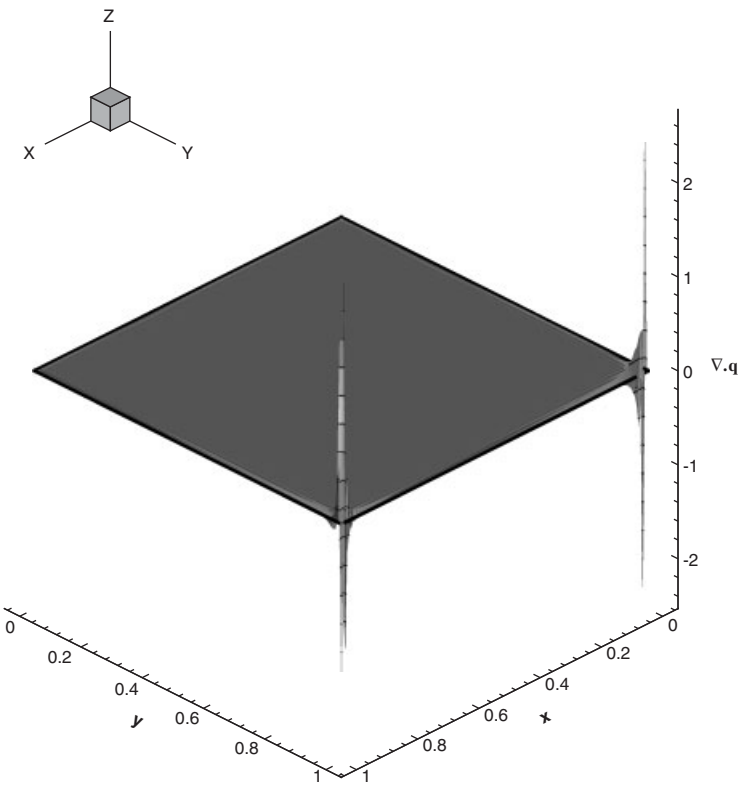

Figure 7. Surface plot of the divergence of velocity for $Re = 1000$ on a 161×161 grid.

defined as

$$E = \frac{1}{2}\int_{\Omega} |\mathbf{q}|^2 \, \mathrm{d}x, \quad Z = \frac{1}{2}\int_{\Omega} \|\omega\|^2 \, \mathrm{d}x, \quad C_{\mathrm{d}} = \frac{1}{Re}\int_0^1 \frac{\partial u}{\partial y} \, \mathrm{d}x$$

where $\mathbf{q} = (u, v)$ and $\omega = \partial v/\partial x - \partial u/\partial y$ is the vorticity. It may be mentioned that in perhaps the only previous example where an HOC method was used to solve this problem using the primitive variable formulation of the N–S equations [1], attempts to compute results for higher Reynolds numbers resulted in oscillations and results were provided only for $Re = 400$. For the cases presented here, no oscillations were seen and as such no under-relaxation was used. However, once Re was increased beyond 4000, oscillations in the pressure values began to appear which, however, can be controlled by using under-relaxation at the boundaries. Also, as expected, the CPU time taken by the primitive variable formulation is much more than what it used to be for the ψ–ω [3] formulation. For example, the CPU time taken for $Re = 1000$ to reach steady state on an 81×81 grid was nearly 1.5 h.

3.3. Test problem 3: the backward-facing step problem

Next we consider the flow over the backward-facing step in a channel which also provides an excellent test case for the accuracy of numerical methods because of the reattachment length being

DOI: 10.1002/fld

Table II. Properties of primary, secondary and tertiary vortices for the lid-driven square cavity from $Re = 100$ to 4000 using (9,5) HOC scheme in primitive variable formulation (results from [18] are given in the parentheses).

		Re						
Vortex	Property	100	400	1000	2000	3200	4000
Primary	$\psi_{\min}$	−0.103 (−0.103)	−0.113 (−0.114)	−0.117 (−0.118)	−0.117 —	−0.119 (−0.120)	−0.119 —
	Location x, y	0.6125, 0.7375 (0.6172, 0.7344)	0.5583, 0.6083 (0.5547, 0.6055)	0.5313, 0.5688 (0.5313, 0.5625)	0.5234, 0.5508 —	0.5156, 0.5391 (0.5165, 0.5469)	0.5195, 0.5391 —
Secondary TL	$\psi_{\max}$	—	—	—	4.20e−5 —	5.65e−4 (7.28e−4)	8.21e−4 —
	Location x, y	—	—	—	0.0234, 0.8750 —	0.0547, 0.8945 (0.0547, 0.8984)	0.0586, 0.9062 —
	H_{L}	—	—	—	0.0364 —	0.0848 (0.0859)	0.0988 —
	V_{L}	—	—	—	0.0812 —	0.1866 (0.2057)	0.1989 —
BL	$\psi_{\max}$	5.51e−7 (1.75e−6)	1.22e−5 (1.42e−5)	2.11e−4 (2.31e−4)	6.74e−4 —	1.03e−3 (9.78e−4)	1.18e−3 —
	Location x, y	0.0250, 0.0378 (0.0313, 0.0391)	0.0500, 0.0500 (0.0508, 0.0469)	0.0813, 0.0750 (0.0859, 0.0781)	0.0859, 0.1016 —	0.0820, 0.1172 (0.0859, 0.1094)	0.0781, 0.1250 —
	H_{L}	0.0625 (0.0781)	0.1167 (0.1273)	0.2125 (0.2188)	0.2695 —	0.2969 (0.2844)	0.3086 —
	V_{L}	0.0625 (0.0781)	0.1083 (0.1081)	0.1688 (0.1680)	0.2188 —	0.2422 (0.2305)	0.2578 —

DOI: 10.1002/fld

BR	$\psi_{\max}$	8.9e−6	6.21e−4	1.68e−3	2.36e−3	2.74e−3	2.85e−3
		(1.25e−5)	(6.42e−4)	(1.75e−3)	—	(3.14e−3)	—
	Location x, y	0.9500, 0.0625	0.8833, 0.1250	0.8625, 0.1124	0.8437, 0.0977	0.8242, 0.0859	0.8164, 0.0820
		(0.9453, 0.0625)	(0.8906, 0.1250)	(0.8594, 0.1094)	—	(0.8125, 0.0859)	—
	H_L	0.1125	0.2667	0.3063	0.3320	0.3516	0.3594
		(0.1328)	(0.2617)	(0.3034)	—	(0.3406)	—
	V_L	0.1250	0.3083	0.3563	0.3867	0.4023	0.4102
		(0.1484)	(0.3203)	(0.3536)	—	(0.4102)	—
Tertiary							
BL	$\psi_{\min}$	−8.52e−8	−2.24e−8	−5.76e−8	−5.58e−8	−7.77e−8	−1.07e−7
		—	—	—	—	—	—
	Location x, y	0.0125, 0.0125	0.0083, 0.0083	0.0124, 0.0062	0.0117, 0.0039	0.0117, 0.0039	0.0117, 0.0039
	H_L	—	—	—	—	—	—
		0.0218	0.0109	0.0155	0.0168	0.0175	0.0206
	V_L	—	—	—	—	—	—
		0.0208	0.0094	0.0077	0.0080	0.0082	0.0096
		—	—	—	—	—	—
BR	$\psi_{\min}$	−1.06e−7	−9.91e−8	−1.98e−7	−1.44e−7	−3.10e−7	−3.717e−7
		—	—	—	—	(−2.52e−7)	—
	Location x, y	0.9875, 0.0125	0.9917, 0.0167	0.9938, 0.0125	0.9922, 0.1172	0.9922, 0.0156	0.9883, 0.0156
		—	—	—	—	(0.9844, 0.0078)	—
	H_L	0.0194	0.0164	0.0139	0.0145	0.0206	0.0235
		—	—	—	—	(0.0254)	—
	V_L	0.0201	0.0200	0.0222	0.0241	0.0320	0.0360
		—	—	—	—	(0.0234)	—
Grid size		81×81	121×121	161×161	257×257	257×257	257×257
		(129×129)	(257×257)	(129×129)	—	(129×129)	—

DOI: 10.1002/fld

Table III. Values of global quantities of energy, enstrophy and drag coefficient at the top for the lid-driven square cavity from $Re = 100$ to 4000 using (9,5) HOC scheme in primitive variable formulation (results from [20] are given in the parentheses).

	Re					
Property	100	400	1000	2000	3200	4000
Kinetic energy	0.037463	0.042095	0.044498 (0.044503)	0.044631	0.045644	0.045993
Enstrophy	11.443	15.917	21.743 (22.424)	28.998	31.676	34.669
Drag coefficient	0.165021	0.058187	0.031915	0.021910	0.016323	0.014255
Grid size	81×81	121×121	161×161 (1024×1024)	257×257	257×257	257×257

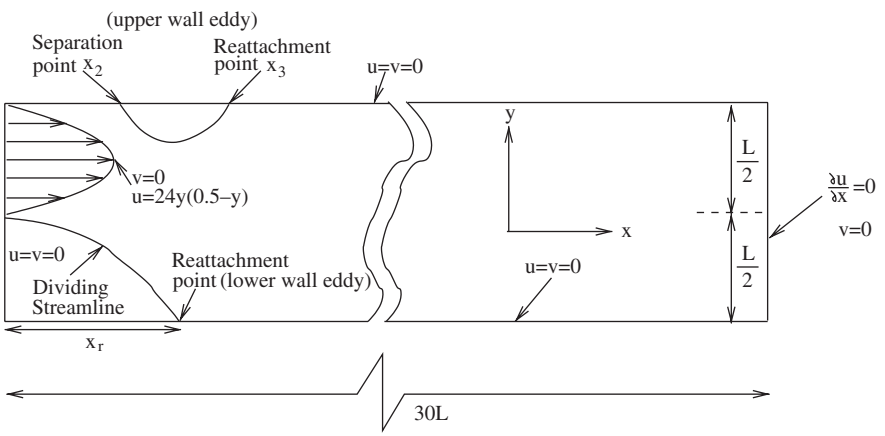

Figure 8. The backward-facing step flow configuration with boundary conditions.

a function of the Reynolds number. Numerical simulations are carried out for Reynolds numbers 100–500 on grid sizes ranging from 1201×41 to 2401×81. The problem configuration is shown in Figure 8. At the inlet, a parabolic velocity profile is usually prescribed [24–29] and the one used here is given by Gartling [28] as $u = 24y(0.5 - y)$, $v = 0$. The downstream boundary conditions are prescribed at a distance of 30 step heights so as to allow the flow to be fully developed. Thus, at the outlet $\partial u/\partial x = 0$ and $v = 0$. At the stationary walls $u = v = 0$. The stream function ψ is post-processed from the values of u and v as in the cavity problem; likewise the numerical criterion for reaching steady state was the same as that of the cavity problem. At the outlet (denoted by the index b), we approximate the values of u arising out of the Neumann boundary condition by the fifth order backward difference formula (see [6])

$$u_{b,j} = \frac{1}{25}\left[48u_{b-1,j} - 36u_{b-2,j} + 16u_{b-3,j} - 3u_{b-4,j} - 12h\left(\frac{\partial u}{\partial x}\right)_{b,j}\right] + O(h^5)$$

DOI: 10.1002/fld

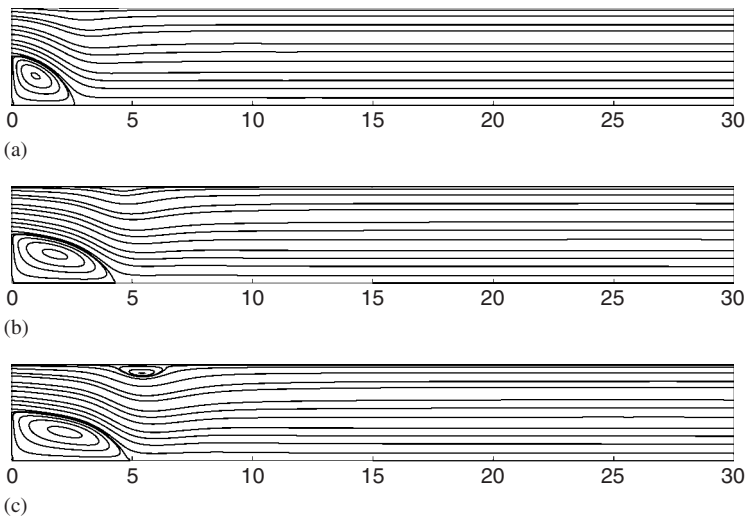

Figure 9. The backward-facing step flow: steady-state streamlines for: (a) $Re = 200$; (b) $Re = 400$; and (c) $Re = 500$.

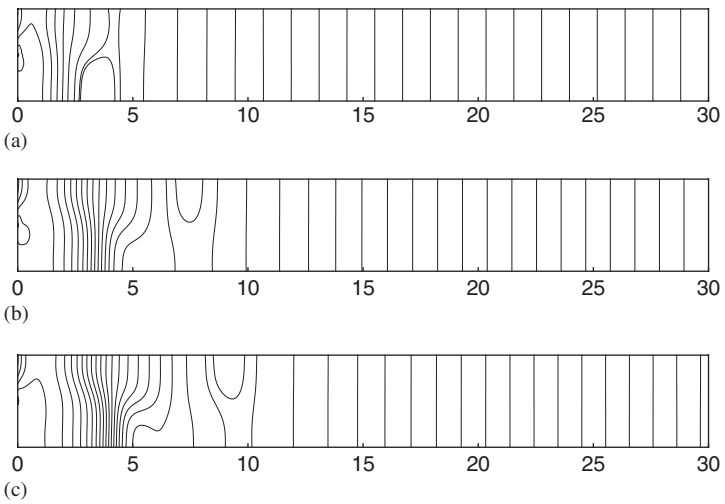

Figure 10. The backward-facing step flow: steady-state pressure contours for: (a) $Re = 200$; (b) $Re = 400$; and (c) $Re = 500$.

Figure 9 shows the steady-state streamline patterns for $200 \leqslant Re \leqslant 500$. One can see a steady increase in the reattachment length with the increase in Re. The formation of a secondary vortex at the upper wall can be seen for $Re = 500$ which was also reported by Sohn [27]. Figure 10 shows the steady-state pressure contours for the same range of Reynolds numbers. As expected, except

DOI: 10.1002/fld

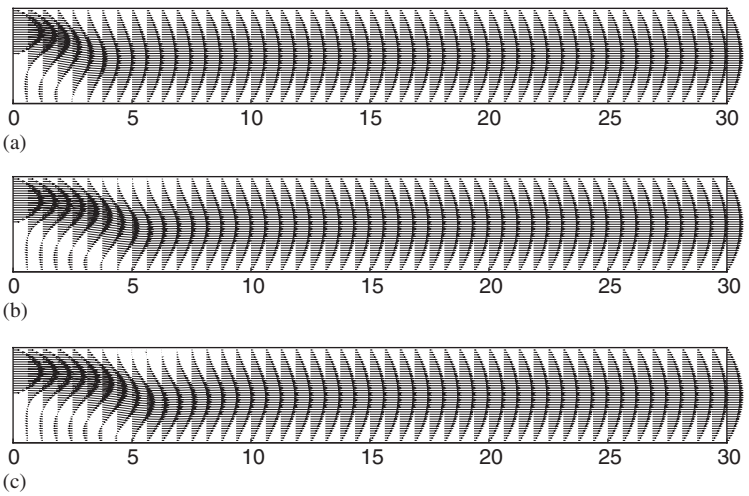

Figure 11. The backward-facing step flow: steady-state relative velocity vector plots for: (a) $Re = 200$; (b) $Re = 400$; and (c) $Re = 500$.

Table IV. Properties of wall eddy for the backward-facing step problem from $Re = 200$ to 500.

Wall	Re	200	400	500
Lower	Eddy centre (x, y)	0.999, −0.200 (0.938, −0.188) [24]	1.800, −0.200 (1.705, −0.188) [24]	2.199, −0.200 (2.079, −0.1874) [24]
	ψ_{value}	−0.0330 (−0.03276) [24]	−0.03412 (−0.03364) [24]	−0.03463 (−0.03373) [24]
	Recirculation length	2.606 (2.633) [24]	4.295 (4.239) [24] (4.32) [29]	4.927 (4.853) [24]
Upper	Eddy centre (x, y)	—	—	5.400, 0.413 (5.438, 0.406) [24]
	ψ_{value}	—	—	0.5005 (0.5005) [24]
	Separation point x_2	—	—	4.255 (4.309) [24]
	Reattachment point x_3	—	—	6.358 (6.555) [24]

in the recirculation zone(s), pressure keeps steadily falling in the downstream direction. Figure 11 exhibit the steady-state relative velocity vector plot. The velocity vector plots give a clear picture of the recirculation zones and the velocity profiles at different streamwise locations, indicating the development of a parabolic profile towards the exit. In these figures, the spacing in the y-direction has been magnified four times for a better resolution. In Table IV, we present the lower and upper wall eddy data and compare them with established results [24, 29], which again are very close.

DOI: 10.1002/fld

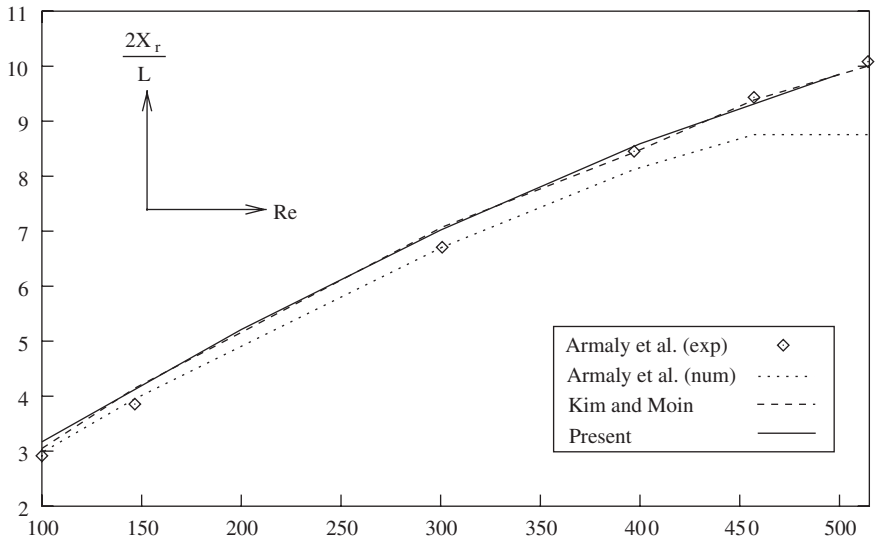

Figure 12. The reattachment length as a function of Reynolds number.

In Figure 12, the reattachment length as a function of Reynolds number is shown against the experimental and computational results of Armaly *et al*. [25] and the numerical results of Kim and Moin [26]. As they give no tabular results, the graphical results were optically scanned to produce the cited quantities. Our results are in excellent agreement with the experimental results of Armaly *et al.* [25] for $100 \leqslant Re \leqslant 500$.

4. CONCLUSION

In this paper, we extend a recently developed (9,5) HOC scheme for transient convection–diffusion to the primitive variable formulations of the N–S equations. This is perhaps the only attempt to solve the N–S equations in the primitive variable form by a transient HOC scheme on a collocated grid. We apply this new approach to the problem of flow decayed by viscosity which has analytical solutions and to compute the time-marching steady-state solution of the famous lid-driven square cavity problem as well as that of the backward-facing step problem. In the first problem, the Dirichlet boundary conditions are used and for the other two, we use the Neumann boundary conditions for pressure. Employing suitable strategies to approximate both types of boundary conditions in conjunction with the (9,5) scheme is seen to produce highly accurate results in all the cases. It is easy to implement and the use of BiCGStab algorithm for solving the algebraic systems arising at every time level makes the implicit procedure computationally efficient even in capturing transient solutions as can be seen from our results in the first problem. As this approach computes unsteady 2-D incompressible viscous flows governed by the N–S equations in the primitive variable formulation, it has the potential to be extended to three dimensions on which we are working at present.

DOI: 10.1002/fld

REFERENCES

1. Mackinnon RJ, Johnson RW. Differential equation based representation of truncation errors for accurate numerical simulation. *International Journal for Numerical Methods in Fluids* 1991; **13**:739–757.
2. Kalita JC, Dalal DC, Dass AK. A class of higher order compact schemes for the unsteady two-dimensional convection–diffusion equation with variable convection coefficients. *International Journal for Numerical Methods in Fluids* 2002; **38**:1111–1131.
3. Kalita JC, Chhabra P. An improved (9,5) higher order compact scheme for the transient two dimensional convection–diffusion equations. *International Journal for Numerical Methods in Fluids* 2006; **51**:703–717.
4. Kalita JC, Dalal DC, Dass AK. Fully compact higher order computation of steady-state natural convection in a square cavity. *Physical Review E* 2001; **64**:1–13.
5. Gresho PM. Some current cfd issues relevant to the incompressible Navier–Stokes equations. *Computational Methods in Applied Mechanical Engineering* 1991; **87**:201–252.
6. Anderson DA, Tannehil JC, Pletcher RH. *Computational Fluid Mechanics and Heat Transfer*. Hemisphere: New York, 1984.
7. Anderson Jr JD. *Computational Fluid Dynamics*. McGraw-Hill: New York, 1995.
8. Abdallah S. Numerical solutions for the incompressible Navier–Stokes equations in primitive variables using a non-staggered grid II. *Journal of Computational Physics* 1987; **70**:193–202.
9. Johnston H, Liu J-G. A finite difference method for incompressible flow based on local pressure boundary conditions. *Journal of Computational Physics* 2002; **180**:120–154.
10. van der Vorst HA. BiCGSTAB: a fast and smoothly converging variant of BiCG for the solution of nonsymmetric linear systems. *SIAM Journal on Scientific Computing* 1992; **13**:631–644.
11. Kelley CT. *Iterative Methods for Linear and Nonlinear Equations*. SIAM: Philadelphia, PA, 1995.
12. Saad Y. *Iterative Methods for Sparse Linear Systems*. PWS: Boston, MA, 1996.
13. Sleijpen GLG, van der Vorst HA. Hybrid bi-conjugate gradient methods for CFD problems. In *Computational Fluid Dynamics Review*, Hafez M, Oshima K (eds). John Wiley & Sons: Chichester, 1995; 457–476.
14. Chorin AJ. Numerical solutions of the Navier–Stokes equations. *Mathematics of Computation* 1968; **95**:745–762.
15. Strikwerda JC. High-order accurate schemes for incompressible viscous flow. *International Journal for Numerical Methods in Fluids* 1997; **24**:715–734.
16. Chen Y-N, Yang S-C, Yang J-Y. Implicit weighted essentially non-oscillatory schemes for the incompressible Navier–Stokes equations. *International Journal for Numerical Methods in Fluids* 1999; **31**:747–765.
17. Ben-Artzi M, Croisille J-P, Fishelov D, Trachtenberg S. A pure-compact scheme for the streamfunction formulation of Navier–Stokes equations. *Journal of Computational Physics* 2005; **205**:640–664.
18. Ghia U, Ghia KN, Shin CT. High re-solution for incompressible Navier–Stokes equation and a multigrid method. *Journal of Computational Physics* 1982; **48**:387–411.
19. Botella O, Peyret R. Benchmark spectral results on the lid-driven cavity flow. *Computers and Fluids* 1998; **27**:421–433.
20. Bruneau CH, Saad M. The 2D lid-driven cavity problem revisited. *Computers and Fluids* 2005; **35**(3):326–348.
21. Shankar PN, Deshpande MD. Fluid mechanics in the driven cavity. *Annual Review of Fluid Mechanics* 2000; **32**:93–136.
22. Bruneau CH, Jouron C. An efficient scheme for solving steady incompressible Navier–Stokes equations. *Journal of Computational Physics* 1990; **89**:389–413.
23. Hou S, Zou Q, Chen S, Doolen G, Cogley AC. Simulation of cavity flow by the Lattice Boltzmann method. *Journal of Computational Physics* 1995; **118**:329–347.
24. Gupta MM, Kalita JC. New paradigm continued: further computations with stream function velocity formulations for solving Navier–Stokes equations. *Communications in Applied Analysis* 2006; **10**(4):461–480.
25. Armaly BF, Durst F, Pereira J, Schonung B. Experimental and theoretical investigation of backward facing step flow. *Journal of Fluid Mechanics* 1983; **127**:473–496.
26. Kim J, Moin P. Application of fractional step method to incompressible Navier–Stokes equation. *Journal of Computational Physics* 1985; **59**:308–323.
27. Sohn J. Evaluation of FIDAP on some classical laminar and turbulent benchmarks. *International Journal for Numerical Methods in Fluids* 1988; **8**:1469–1490.
28. Gartling DK. A test problem for outflow boundary conditions-flow over a backward facing step. *International Journal for Numerical Methods in Fluids* 1990; **11**:953–967.
29. Srinivasan K, Rubin SG. Segmented multigrid domain decomposition procedure for incompressible viscous flows. *International Journal for Numerical Methods in Fluids* 1992; **15**:1333–1355.

DOI: 10.1002/fld